

# Spacetime-spectral analysis of flowfields

Vilas J. Shinde<sup>†</sup>

Department of Aerospace Engineering,  
Mississippi State University, Mississippi State, MS 39762, USA

(Received xx; revised xx; accepted xx)

The classical Fourier analysis of a time signal, in the discrete sense, provides the frequency content of signal under the assumption of periodicity. Although the original signal can be exactly recovered using an inverse transform, the time dependence of the spectrum remains inaccessible. There exist various time-frequency analysis techniques, such as the short time fast Fourier transform and wavelets, but those are fundamentally limited in achieving high resolution in both the time and frequency domains concurrently. For spatiotemporal flowfields, the frequency based modal decompositions generally provide spatial modes with a temporal counterpart that evolves at a constant frequency. However, an accurate time-local spectral contribution and its variation over time are highly desired to better understand the intermittent/extreme events, for instance, in turbulent flowfields. To this end, this paper presents a spectral mode decomposition that yields spectral-space and spectral-time modes, where the latter along with the associated spectral energies provide a spectrogram that is at the resolution of flowfields. The spectral modes get both the frequency and energy ranks. The numerical examples demonstrate the use of technique not only in spacetime-frequency analysis but also in reduced-order modeling and denoising applications.

**Key words:** Spatiotemporal fields, Time frequency analysis, Fourier transform, Modal decomposition techniques

## 1. Introduction

Spatiotemporal fields are omnipresent in all branches of sciences, and for that matter humanities. The study of physical phenomena typically involves a set of variables (*e.g.*, velocity, pressure, concentration, etc. in fluid sciences) with a spatial distribution that evolves in time; above all, it includes understanding, analysis, modeling, and prediction of these spatiotemporal variable fields. In fluid mechanics, turbulence is a prime example that exhibits complex spatiotemporal flowfields. Needless to say, turbulence plays a key role in transport phenomena, environmental flows, plasma physics, to mention a few. A turbulent flow is characterized by the presence of a wide range of length/time scales, comprising complex interactions across the scales (Batchelor 1953; Tennekes & Lumley 1972). Further, it manifests spatiotemporal coherence, energy bursts, and intermittent/extreme events whose identification and understanding are of critical importance from practical standpoint. To this end, the spectral mode decomposition (SMD) presented in this paper facilitates the identification of spectral spatial coherence and its non-sinusoidal temporal dynamics, providing a highly resolved spectrogram.

Time-frequency analysis methods have been extensively used in signal processing,

<sup>†</sup> Email address for correspondence: vshinde@ae.msstate.edu

primarily to identify time-local spectral events. A more popular Fourier transform (FT) when applied to the entire time domain provides overall frequency contributions; however, the time-local presence of frequencies is not retrieved. The Fourier transform consists of a constant amplitude sine/cosine waves, thus the time varying spectral information, *i.e* spectrogram, remains inaccessible. The spectrogram is commonly obtained by employing a short time Fourier transform (STFT) repeatedly. Generally, STFT spectrogram provides only the spectral magnitudes, losing track of the phase information; the reconstruction of the original signal based on spectrogram is an intricate process. To account for the frequency variation over time, the sine/cosine waves are modulated to change over time, leading to wavelets. It employs a specific multi-frequency kernel, known as a mother wavelet, to identify the time-local spectral presence. The more common Morlet is a combination of the sine and Gaussian functions. Wavelet transforms are effective for non-stationary signals, and are particularly effective with non-harmonic functions. Among several limitations of time-frequency analyses (Cohen 1995; Morales & Bowers 2022), the limitation of trade-off between the time and frequency can be significant, as resolving the lower frequencies require longer time duration. In addition, the time-frequency analyses are commonly employed to local/sparse spatial information and seldom to extract a highly-resolved spatial coherence.

With the availability of scale-resolved experimental and numerical simulations of turbulent flows, numerous modal decomposition techniques have emerged in order to extract the spatial/temporal coherence in seemingly chaotic fluid motions (Rowley & Dawson 2017; Taira *et al.* 2017). These techniques differ in their definition of the coherence and ranking of modes, as well as specific physical characteristics of their dynamics. The more fundamental modal decomposition techniques include: Fourier decomposition, proper orthogonal decomposition (POD) (Lumley 1970; Sirovich 1987), and dynamics mode decomposition (DMD) (Schmid 2010; Rowley *et al.* 2009). A common factor among all modal decomposition techniques is that they decompose spatiotemporal flowfields into spatial coherent patterns and their associated temporal dynamics. Although essentially these techniques build on Fourier transform/eigen-/singular-value decompositions, these bring out distinct spatiotemporal dynamics that pertains to their construct.

Fourier spatial modes represent the spectral weights at specific frequency and the corresponding time coefficients are monotones of the associated frequencies. By definition, the temporal coefficients form an orthogonal set of temporal modes, whereas the spatial Fourier modes need not be orthogonal. POD is another popular technique that distills most energetic spatial/temporal modes for a given rank which is based on the energy. It employs the eigenvalue decomposition, leading to bi-orthonormal sets of space and time modes. Importantly, the POD modes may (and generally) comprise multiple frequencies in their spatiotemporal dynamics. The variance associated with the modes, *i.e.* the modal energy, defines the mode rank. Lastly, the DMD procedure seeks for spatial modes at a specific frequency and associated growth/decay rate. The temporal modes of DMD exhibit a single frequency that is growing or decaying in time at a constant rate. Similar to Fourier modes, the time modes are orthogonal by definition, whereas the spatial DMD modes need not be orthogonal. For stationary flows, the DMD modes show sustained dynamics or zero growth rate, similar to the Fourier modes. Nonetheless, the construct of Fourier and DMD modes are characteristically different; the Fourier modes comprise a constant spectral spatial coherence, while the DMD modes exhibit spectral spatial coherence that grows/decays with time. The FT/POD/DMD and their variants have been extremely useful in decoding the spatiotemporal dynamics, size reduction, and constructing efficient predictive models of complex turbulent flows.

The two classes of techniques, namely the time-frequency analysis and the modal

decomposition, separately seek to obtain, respectively, a well-resolved time-varying spectral contribution, and a converged spatial coherent patterns with associated temporal dynamics. In this regard, a modal decomposition technique with time-varying spectral dynamics is highly desired in order to investigate the spatiotemporal flowfields in a unified manner. The frequency based modal decomposition methods, i.e. FT, DMD, and spectral variants of POD (Lumley 1967; Towne *et al.* 2018), provide spatial modes corresponding to a unique frequency and associated temporal coefficients that evolve at a constant frequency. In turbulent spatiotemporal flowfields, it is crucial to know the time-local spectral contribution and its variation over time, which need not be at a fixed frequency that is associated with the mode (Sieber *et al.* 2016; Nekkanti & Schmidt 2021). In this quest, a spectral mode decomposition procedure is developed in this paper, where the time coefficients that are associated with the spectral spatial modes capture the exact time-local modal contribution and its variation over time. The spectral spatial modes are essentially the Fourier modes at a unique frequency and with a specific spectral energy, which provides another measure for the modal rank.

The proposed SMD method for the spacetime-frequency analysis of flowfields is demonstrated considering the following three numerical examples with increasing level of complexity: 1. transitional lid-driven cavity (LDC) at Mach 0.5 and Reynolds number  $Re_L = 12000$  based on the cavity length  $L$ , 2. a turbulent LDC at Mach 0.5 and  $Re_L = 15000$ , and 3. a fully turbulent shockwave boundary layer interaction (SBLI) at Mach 2.7 and Reynolds number  $Re_{\delta_{in}} = 54600$  based on the inflow boundary layer thickness  $\delta_{in}$ . In the following section (Sec. 2), a mathematical framework of Fourier transform and the SMD procedure in a matrix form are presented. Next, the numerical examples are presented in Sec. 3, and Sec. 4. A potential use of SMD in full/partial flow reconstruction and denoising applications is explored in the next section (Sec. 5). Some concluding remarks are provided in Sec. 6.

## 2. Mathematical framework

### 2.1. Spacetime flowfields and Fourier transform

A spectral description of fluid flows evokes complex vector spaces that provide suitable mathematical framework to handle basis functions with infinite degrees of freedom. Here, we consider a vector space  $\mathbf{E}$  as a  $d$ -dimensional point space with a coordinate system and a reference frame, on which the Euclidean space with  $\mathbb{C}^{d=3}$  can be realized by considering an orthonormal basis. A complex spacetime flowfield,  $\mathbf{u}$ , in a suitable closed domain  $\mathbf{X} \subseteq \mathbf{E}$  in  $\mathbb{R}^{d=3}$  may be represented through the mapping

$$\mathbf{u} : \mathbf{X} \times [0, T] \rightarrow \mathbb{C}^3 : (\mathbf{x}, t) \mapsto \mathbf{u}(\mathbf{x}, t) \text{ with } \mathbf{x} \in \mathbf{X},$$

where  $t$  is an instant from the total time  $T \subset \mathbb{R}$ . The definition of flowfields include all physical quantities (scalar, vector or tensor) that are expressed at each instant and at every spatial location. Note that the real flowfields, *e.g.*  $\mathbf{u} \in \mathbb{R}^3$ , over a complex space consist zero imaginary parts.

The complex inner product space can be given by the map:

$$\langle \cdot, \cdot \rangle : \mathbf{X} \times \mathbf{X} \rightarrow \mathbb{C}^3,$$

satisfying the properties, namely, linearity, conjugate symmetry, and positive definitiveness. Thus, a complex inner product  $\langle \mathbf{u}, \mathbf{u} \rangle > 0$  for a non-zero  $\mathbf{u}$ , and the complex norm  $\|\mathbf{u}\| = \sqrt{\langle \mathbf{u}, \mathbf{u} \rangle}$  for any  $\mathbf{u}$ , providing its magnitude. The inner product over space utilizes spatial weights, accounting for the non-uniformity of the spatial domain. The flowfields

are assumed to be square integrable, i.e.,  $\|\mathbf{u}\|^2 < \infty$ , providing a suitable space for the Fourier transform.

The Fourier transform of,  $\mathbf{u}(\mathbf{x}, t)$ , on a time line can be defined as,

$$\mathbf{s}(\mathbf{x}, f) = \int_{\mathcal{T}} \mathbf{u}(\mathbf{x}, t) e^{-i2\pi f t} dt, \quad (2.1)$$

where  $i = \sqrt{-1}$ ,  $\mathbf{s}(\mathbf{x}, f) \in \mathbb{C}^{d=3}$  is a complex valued flowfield, and  $f$  is a frequency from the entire spectrum  $\mathcal{F} \subset \mathbb{R}$ . The inverse Fourier transform is then defined as,

$$\mathbf{u}(\mathbf{x}, t) = \int_{\mathcal{F}} \mathbf{s}(\mathbf{x}, f) e^{i2\pi f t} df, \quad (2.2)$$

returning the original flowfield,  $\mathbf{u}(\mathbf{x}, t)$ . The conservation of energy in Fourier (time-frequency) transformation is ensured by the Parseval-Plancherel theorem,

$$\int_{\mathcal{T}} |\mathbf{u}(\mathbf{x}, t)|^2 dt = \int_{\mathcal{F}} |\mathbf{s}(\mathbf{x}, f)|^2 df, \quad (2.3)$$

which states that the total time-integrated energy is equal to the total frequency-integrated (spectral) energy of a function. In the context of spacetime flowfields, we can rewrite Eq. 2.3 as

$$\begin{aligned} \int_{\mathcal{T}} \left( \int_{\mathcal{X}} |\mathbf{u}(\mathbf{x}, t)|^2 d\mathbf{x} \right) dt &= \int_{\mathcal{F}} \left( \int_{\mathcal{X}} |\mathbf{s}(\mathbf{x}, f)|^2 d\mathbf{x} \right) df \\ &= \int_{\mathcal{F}} \lambda_f df \end{aligned} \quad (2.4)$$

where  $\lambda_f$  is a space-integrated total spectral energy at frequency  $f$ .

The factors such as the discrete version of Fourier transform, the fast Fourier transform (FFT) algorithm, and its ability to analyze/reconstruct complex flowfields have been instrumental in the popularity of Fourier transform. To be consistent with the discrete formulation, we present the development of the spectral mode decomposition in the matrix form in the following section.

## 2.2. Spectral mode decomposition

Let us consider a tensor  $\mathbf{U}$  that comprises the spacetime flowfields, e.g. the velocity vector  $\mathbf{u}(\mathbf{x}, t)$  with the discrete time  $t \in [0, T]$ , such that  $t = \{t_1, t_2, \dots, t_n\}$ . Similarly, the space coordinate vector  $\mathbf{x}$  is considered to be discrete of size  $m$ , thus  $\mathbf{U} \in \mathbb{C}^{m \times n}$ . Let  $\mathcal{F} \in \mathbb{C}^{n \times n}$  be the discrete Fourier transform operator that transforms the spacetime flowfields into space-frequency fields as,

$$\mathbf{S} = \mathbf{U} \mathcal{F}, \quad (2.5)$$

where the columns of  $\mathcal{F}$  form an orthonormal Fourier basis. The inverse operation can be performed using an adjoint  $\mathcal{F}^\dagger \in \mathbb{C}^{n \times n}$  of the Fourier transform operator  $\mathcal{F}$  as,

$$\mathbf{U} = \mathbf{S} \mathcal{F}^\dagger, \quad (2.6)$$

Also, for an unitary  $\mathcal{F}$ :

$$\mathcal{F}^\dagger \mathcal{F} = \mathbf{I}, \quad (2.7)$$

where  $\mathbf{I} \in \mathbb{R}^{n \times n}$  is an identity matrix. The forward and inverse Fourier transform matrices, for  $\varpi = e^{(i2\pi/n)}$ , are respectively given by:

$$\mathcal{F} = \begin{bmatrix} \cdot & \cdot & \cdots & \cdot & \cdot \\ \cdot & \cdot & \cdots & \cdot & \cdot \\ \vdots & \vdots & \frac{\varpi^{jk}}{\sqrt{n}} & \vdots & \vdots \\ \cdot & \cdot & \cdots & \cdot & \cdot \\ \cdot & \cdot & \cdots & \cdot & \cdot \end{bmatrix}, \text{ and } \mathcal{F}^\dagger = \begin{bmatrix} \cdot & \cdot & \cdots & \cdot & \cdot \\ \cdot & \cdot & \cdots & \cdot & \cdot \\ \vdots & \vdots & \frac{(\varpi^*)^{jk}}{\sqrt{n}} & \vdots & \vdots \\ \cdot & \cdot & \cdots & \cdot & \cdot \\ \cdot & \cdot & \cdots & \cdot & \cdot \end{bmatrix}, \quad (2.8)$$

where  $(j = 0, 1, \dots, n-1)$  and  $(k = 0, 1, \dots, n-1)$  are the running indices that provide the elements of the matrices. For instance, the first and last elements of the matrices have exponents  $j, k = 0$  and  $j, k = (n-1)$ , respectively.  $\varpi^*$  is the complex conjugate of  $\varpi$ , i.e.,  $\varpi^* = e^{(-i2\pi/n)}$ .

The spatial spectral fields, *i.e.* the rows of  $\mathbf{S} \in \mathbb{C}^{m \times n}$ , can be normalized to obtain the spectral modes as

$$\boldsymbol{\Phi} = \mathbf{S} \boldsymbol{\Lambda}^{-\frac{1}{2}}, \quad (2.9)$$

where  $\boldsymbol{\Lambda} = \text{diag}\{\lambda_1, \lambda_2, \dots, \lambda_n\} \in \mathbb{R}^{n \times n}$  is a diagonal matrix with spectral energies  $(\lambda_l)$ . The spectral energies are given by the diagonal of  $\mathbf{S}^\dagger \mathbf{S} = \boldsymbol{\Lambda}$ . As noted before, the inner product over the space accounts for the non-uniformity of the computational grid/spatial domain. The matrix  $\boldsymbol{\Phi} \in \mathbb{C}^{m \times n}$  comprises a set of complex spectral space modes, where the modes form a basis,  $\boldsymbol{\Phi}^\dagger \boldsymbol{\Phi} = \mathbf{I}$ , that is normalized but not necessarily orthogonal. The spacetime flowfields in,  $\mathbf{U}$ , can be expressed as:

$$\mathbf{U} = \boldsymbol{\Phi} \boldsymbol{\Lambda}^{\frac{1}{2}} \boldsymbol{\Psi}^\dagger, \quad (2.10)$$

where  $\boldsymbol{\Psi} \in \mathbb{C}^{n \times n}$  is a complex matrix comprising temporal coefficients that correspond to the spectral space modes  $\boldsymbol{\Phi}$ . Furthermore, the time-coefficient matrix,  $\boldsymbol{\Psi}$ , also forms a spectral time basis as  $\boldsymbol{\Psi}^\dagger \boldsymbol{\Psi} = \mathbf{I}$ , where the spectral time modes are also normalized but not necessarily orthogonal. The spectral time modes can be obtained as,

$$\boldsymbol{\Psi} = \mathbf{U}^\dagger \boldsymbol{\Phi} \boldsymbol{\Lambda}^{-\frac{1}{2}}. \quad (2.11)$$

The total energy of flowfields at each space-point can be given by the diagonal of the matrix multiplication:

$$\mathbf{U} \mathbf{U}^\dagger = (\boldsymbol{\Phi} \boldsymbol{\Lambda}^{\frac{1}{2}} \boldsymbol{\Psi}^\dagger) (\boldsymbol{\Phi} \boldsymbol{\Lambda}^{\frac{1}{2}} \boldsymbol{\Psi}^\dagger)^\dagger \quad (2.12)$$

$$\begin{aligned} &= \boldsymbol{\Phi} \boldsymbol{\Lambda}^{\frac{1}{2}} \boldsymbol{\Psi}^\dagger \boldsymbol{\Psi} \boldsymbol{\Lambda}^{\frac{1}{2}} \boldsymbol{\Phi}^\dagger \\ &= \boldsymbol{\Phi} \boldsymbol{\Lambda}^{\frac{1}{2}} \boldsymbol{\Lambda}^{\frac{1}{2}} \boldsymbol{\Phi}^\dagger \end{aligned}$$

$$\begin{aligned} \boldsymbol{\Phi}^\dagger \mathbf{U} \mathbf{U}^\dagger \boldsymbol{\Phi} &= \boldsymbol{\Lambda} \\ \boldsymbol{\Lambda}^{\frac{1}{2}} \boldsymbol{\Psi}^\dagger \boldsymbol{\Psi} \boldsymbol{\Lambda}^{\frac{1}{2}} &= \boldsymbol{\Lambda} \\ \boldsymbol{\varphi}^\dagger \boldsymbol{\varphi} &= \boldsymbol{\Lambda} \end{aligned} \quad (2.13)$$

Equation 2.13 affirms the Parseval-Plancherel's energy theorem, where the total space-integrated energy of a flowfield is conserved in the time-frequency transformations. The total space-time-integrated energy of a flowfield can be given as  $\text{tr}(\boldsymbol{\Lambda}) = \sum_f \lambda_f$ . The matrix  $\boldsymbol{\varphi} \in \mathbb{C}^{n \times n}$  comprises non-normalized time modes, where each mode corresponds to a spectral spatial mode at a unique frequency. The squared norm of the individual modes of  $\boldsymbol{\varphi}$  also provides the spectral energies, *i.e.*  $\|\boldsymbol{\varphi}_f\|_F^2 = \lambda_f$ , and notably this gives access to the temporal variation of the spectral energies - the spectrogram.

The SMD procedure transforms the spatio-temporal flowfields of  $\mathbf{U}$  into a set of

complex space ( $\Phi$ ) and time ( $\Psi$ ) modes, and associated energies ( $\lambda_f$ ). The space modes consist of normalized magnitude, energy, or power spectral density (PSD) fields that are obtained by performing Fourier transform, where each mode manifests a spatial distribution of the spectral content at a unique frequency. The corresponding time mode exhibits a temporal distribution of the spectral content of that mode, which need not be uniform over the entire time span. This enables the non-normalized time modes of,  $\varphi$ , to provide the temporal variation of the spectral energy associated with each mode, leading to a highly (time-frequency) resolved spectrogram. Alternatively, the non-normalized time modes  $\varphi$  can be obtained by projecting the flowfields on the absolute spectral modes, following Eq. 2.11 as:

$$\varphi = U^\dagger |\Phi|. \quad (2.14)$$

In the following sections, we demonstrate the use of SMD for spacetime-frequency analysis of spatiotemporal flowfields, in terms of high-fidelity direct numerical/large eddy simulations (DNS/LES) databases of flows with increasing complexity.

### 3. Lid-driven cavity flow

The lid-driven cavity flow is a canonical case study in fluid dynamics. It is simple in terms of its geometry yet it exhibits a fairly complex flow physics. The flow remains steady until a critical value of Reynolds number, and becomes unsteady via Hopf bifurcation (Ghia *et al.* 1982; Shen 1991; Ramanan & Homsy 1994). In the post-bifurcation regime, the flow three-dimensionality alongside the end-wall effects become significant from the flow physics viewpoint (Koseff *et al.* 1983; Sheu & Tsai 2002; Albensoeder & Kuhlmann 2005; Lopez *et al.* 2017). Nonetheless, DNS of two-dimensional LDC serves as a canonical benchmark for many efforts (Bruneau & Saad 2006; Shinde & Gaitonde 2021; Shinde 2025b), including the present. In addition, the flow compressibility is known to have stabilizing effect on the LDC flow dynamics (Bergamo *et al.* 2015; Ohmichi & Suzuki 2017; Ranjan *et al.* 2020; Shinde & Gaitonde 2021; Shinde 2025b), increasing the value of the critical Reynolds number. For Mach 0.5, the critical Reynolds number based on the cavity length is  $Re_L \approx 11000$  (Ohmichi & Suzuki 2017; Shinde & Gaitonde 2021; Shinde 2025b).

To demonstrate the use of SMD, we consider the LDC flow at post-critical Reynolds numbers of  $Re_L = 12000$  and  $Re_L = 15000$ , anticipating a few frequency dominant unsteadiness at the lower Reynolds number case and an increased level of turbulence at the higher Reynolds number case. The computational details on the geometry and grid convergence are provided in an appendix of Shinde & Gaitonde (2021). Here we utilize a database that has a LDC flow domain discretized using a grid resolution of  $501 \times 501$ , while the time domain has 1000 snapshots at  $\delta t = 0.05$ . This leads to the frequency resolution of  $\delta f = 0.02$  over  $f \in [0, 10]$ , set by the Nyquist criterion.

The solution vector, of the full compressible Navier-Stokes equations, comprises the three velocity components, the pressure, and the density of the flow. For the SMD analysis here, we consider spacetime flowfields of the horizontal velocity ( $u_1$ ). An instance of the horizontal velocity for  $Re = 12000$  is displayed in Fig. 1(a). At this post-critical Reynolds number, referring to the spectral energy graph of Fig. 1(b), the LDC flow exhibits a prominent spectral peak at  $f = 0.4$  and its two super-harmonics at  $f = 0.8$ , and  $f = 1.2$ . Interestingly, the stability analysis of a pre-critical (Shinde & Gaitonde 2021; Shen 1991; Ohmichi & Suzuki 2017) LDC baseflow at  $Re_L = 7000$  and a post-critical (Shinde 2025b) LDC flow at  $Re_L = 12000$  indicate that the first and second instability modes have

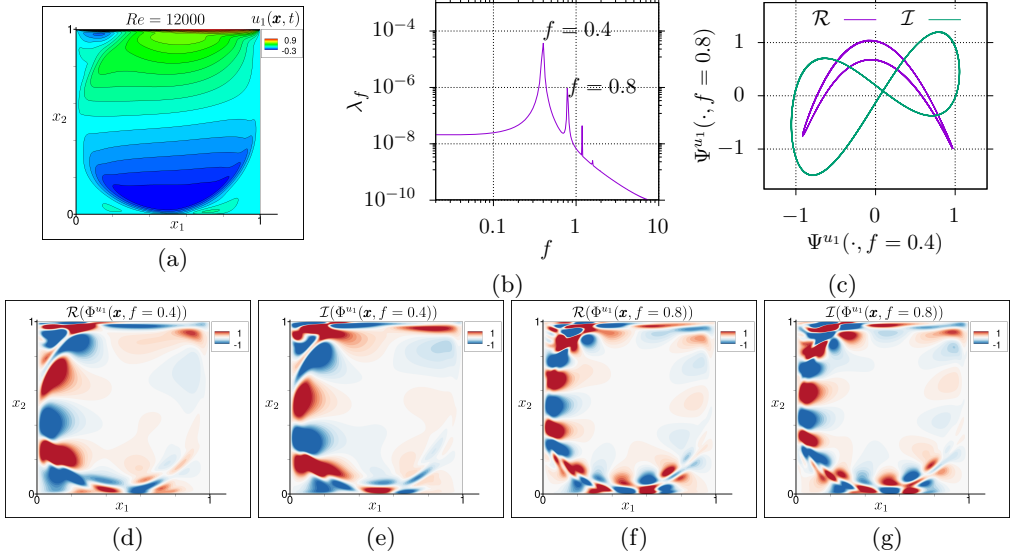


FIGURE 1. Spectral mode decomposition of lid-driven cavity at  $Re = 12000$ . (a) An instantaneous DNS flowfield of the horizontal velocity component. (b) Spectral energies of the SMD modes. (c) Phase portraits of the SMD time-modes. (d) Real part of the spatial spectral mode at  $f = 0.4$ . (e) Imaginary part of the spatial spectral mode at  $f = 0.4$ . (d) Real part of the spatial spectral mode at  $f = 0.8$ . (e) Imaginary part of the spatial spectral mode at  $f = 0.8$ .

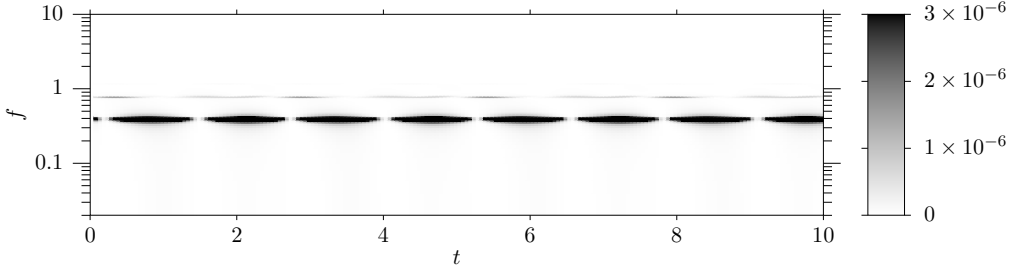


FIGURE 2. Spectrogram,  $|\varphi_f|^2$ , of lid-driven cavity flow at  $Re = 12000$ .

frequencies of  $f = 0.13$ ,  $f = 0.26$ , respectively. Here, at  $Re = 12000$ , the most energetic SMD mode appears at the third super-harmonic of the first instability mode frequency.

The spatial modes ( $\Phi^{u_1}(\mathbf{x}, f = 0.4)$  and  $\Phi^{u_1}(\mathbf{x}, f = 0.8)$ ) that correspond to the spectral energy peaks of Fig. 1(b) are displayed in Fig. 1(d) through (g) in terms of their real and imaginary parts. The spatial shift in the modal peaks of the real and imaginary parts for the both modes at  $f = 0.4$  (Fig. 1(d) and (e)) and  $f = 0.8$  (Fig. 1(f) and (g)) is evident. As expected, the peaks/troughs of the spatial modes are distributed along the shear layer region of the LDC, consistent with the energy based POD and the frequency/growth-rate based DMD modes (Shinde & Gaitonde 2021). The corresponding temporal modes ( $\Psi^{u_1}(t, f = 0.4)$  and  $\Psi^{u_1}(t, f = 0.8)$ ) are displayed in Fig. 1(c) in terms of phase portraits. The figure shows both the real and imaginary parts of the time-modes, exhibiting limit cycle oscillations (LCO). Clearly, the LDC flow at Reynolds number 12000 consists of a primary frequency and its sub/super-harmonics in totality.

A spectrogram of the LDC at  $Re = 12000$  in terms of the non-normalized time-modes  $\varphi_f$  is displayed in Fig. 2. Note that the time and frequency resolutions/extents are exactly

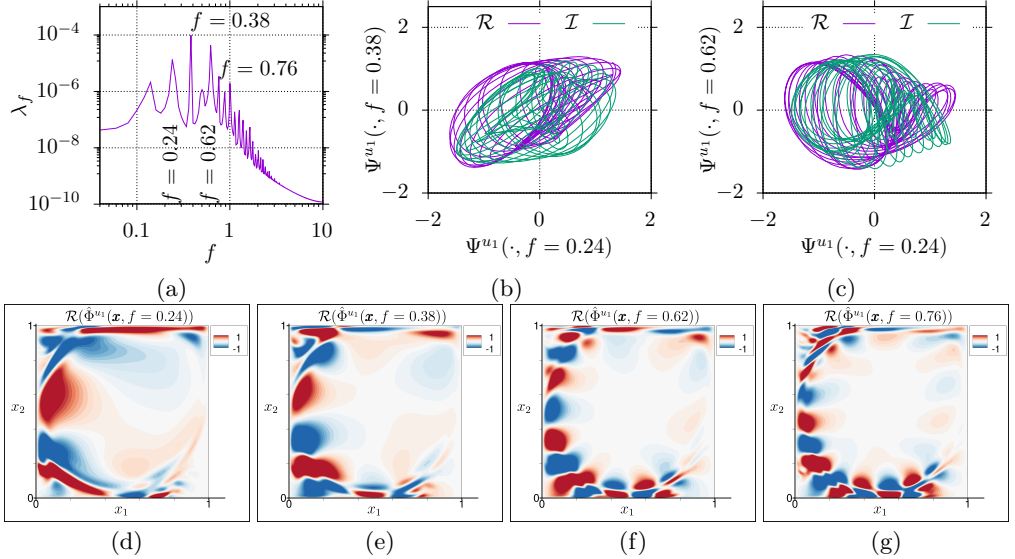


FIGURE 3. Spectral mode decomposition of lid-driven cavity at  $Re = 15000$ . (a) Spectral energies of the SMD modes. (b) Phase portraits of the SMD time-modes at  $f = 0.24$  versus  $f = 0.38$ . (c) Phase portraits of the SMD time-modes at  $f = 0.24$  versus  $f = 0.62$ . (d) Real parts of the spatial spectral mode at  $f = 0.24$ . (e) Real part of the spatial spectral mode at  $f = 0.38$ . (d) Real part of the spatial spectral mode at  $f = 0.62$ . (e) Real part of the spatial spectral mode at  $f = 0.76$ .

same as the input flowfields. The figure shows two distinct peaks at  $f = 0.4$  and  $f = 0.8$  varying over the entire time period. The time variation of the  $f = 0.8$  frequency exhibits some modulation over time (with a duration of  $\approx 3$ ). Furthermore, its peaks are not aligned with the peaks of frequency  $f = 0.4$ . Although the frequency  $f = 0.8$  is a higher harmonic of  $f = 0.4$ , there exists a phase dynamics between the two. Also, note that the spectral of energies of Fig. 1(b) are the aggregate time-sum of the spectrogram of Fig. 2.

Next, we consider the LDC flow at a higher Reynolds number of  $Re_L = 15000$ , increasing the level of flow turbulence. The spectral modal energies are displayed in Fig. 3(a), where additional frequency peaks are evident. The frequency peaks at  $f = 0.38$  and  $f = 0.76$  are reminiscent of the  $f = 0.4$  and  $0.8$  of the LDC flow at  $Re_L = 12000$ . The increase of Reynolds number has introduced two energetically prominent modes at  $f = 0.24$  and  $f = 0.62$ . The energy ranks of these modes in the decreasing order are as follows:  $f = 0.38, f = 0.62, f = 0.24$ , and  $f = 0.76$ . The next peak in the energy rank is at  $f = 0.14$ , which corresponds to the instability mode typically predicted by the stability analysis techniques (Ohmichi & Suzuki 2017; Shinde 2025b). In addition, there exist several higher frequency peaks, albeit at lower spectral energy.

The spatial modes corresponding to the spectral peaks of Fig. 3(a) are displayed in Fig. 3(d) through (g). These figures show the real parts of the modes at  $f = 0.24$ ,  $f = 0.38$ ,  $f = 0.62$ , and  $f = 0.76$ , respectively. The modal structure of these SMD modes, to a great degree, resembles with the POD and DMD modes of the same flow configuration (*i.e.*, LDC at Mach 0.5 and  $Re_L = 15000$ ) that are presented in Shinde & Gaitonde (2021). In contrast to the POD and DMD modes, the SMD modes exhibit a unique frequency and also an associated unique energy rank. The modal structure closely relates to that of DMD modes at the same frequency; however, by design the DMD modes have an associated growth/decay rate and not the energy ranking. For instance, the DMD

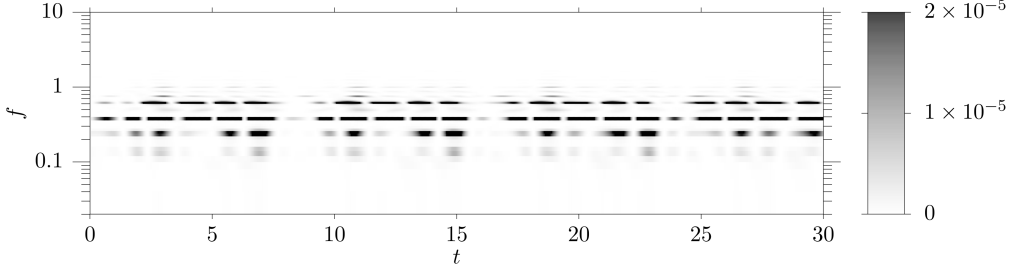


FIGURE 4. Spectrogram,  $|\varphi_f|^2$ , of lid-driven cavity flow at  $Re = 15000$ .

mode at  $f = 0.37$  has the spatial structure of Fig. 3(e) (also shown in Fig. 5(b) of Shinde & Gaitonde (2021)) with an associated growth rate of zero, similar to several other DMD modes those constitute the stationary flow. In SMD, the energy ranking helps extracting the modes in a straightforward manner. The energy based POD modes that have similar temporal dynamics tend to exhibit the modal structure that is similar to the SMD modes; however, by design the POD procedure is not concerned about the frequency association of the POD modes. In general, the modal structures at higher frequency modes consist of smaller lobes of peaks and troughs (Fig. 3d through 3g), which are representative of the smaller scales of flow turbulence.

The phase portraits of the spectral time modes that correspond to  $f = 0.24$ ,  $f = 0.38$ , and  $f = 0.62$  are shown in Fig. 3(b) and (c) for both the real and imaginary parts. The chaotic yet organized nature of these spectral modes is evident in the figures. The LDC flow at  $Re_L = 15000$  has evolved from the LCO at  $Re_L = 12000$  to more nonlinear oscillations of the low-rank high-energy SMD time-modes. The temporal variation of a spectral time mode ( $\Psi_f^{u_1}$ ) follows the contribution of the corresponding spectral spatial mode ( $\Phi_f^{u_1}$ ) at that particular time. Thus, the time oscillations of the these time modes need not exhibit a regular period that corresponds to the modal frequency, and may comprise various frequencies pertaining to the flow physics. This is analogous to the POD, where the temporal modes may comprise multi-frequency oscillations in order to seek spatial modes that are optimal in energy.

The spectrogram of LDC flow at  $Re_L = 15000$  is shown in Fig. 4 in terms of the non-normalized spectral time modes,  $\varphi_f$ . The instantaneous time variation of the prominent frequencies at, namely,  $f = 0.24$ ,  $f = 0.38$ , and  $f = 0.62$  is evident in the spectrogram. It also shows the weaker peaks of spectral energy at  $f = 0.13$  and  $f = 0.76$ . To some degree, the energy ranking of the spectral modes is also evident in the spectrogram. Clearly, the  $\Phi_{f=0.38}^{u_1}$  is the highest energy mode with a consistent presence in the flow. Instantaneously, the peaks of  $f = 0.24$  appear stronger but less regular, in terms of their strength, as compared to the peaks of  $f = 0.62$ , which are relatively more consistent. Thus, the total spectral energy of Fig. 3(a) displays the modes at  $f = 0.62$  and  $f = 0.24$  as the second and third in the energy rank, respectively.

The spectrogram of Fig. 4 also highlights the relative temporal organization of the energy contribution by these modes. On the time axis, there are zones of overall lower spectral energy, *e.g.* over time  $7.5 \lesssim t \lesssim 9.5$ . For increasing time ( $t \geq 9.5$ ), the spectral energy peaks at the previously noted frequencies appear with varying magnitudes in a sequence as follows: a weak peak of  $f = 0.62$ , a strong peak of  $f = 0.38$ , a weak peak at 0.24, a much weaker peak at 0.13, a strong peak at 0.62, a strong peak at 0.38, a strong peak at 0.24, a weak peak of  $f = 0.13$ , and so on. The temporal organization of these

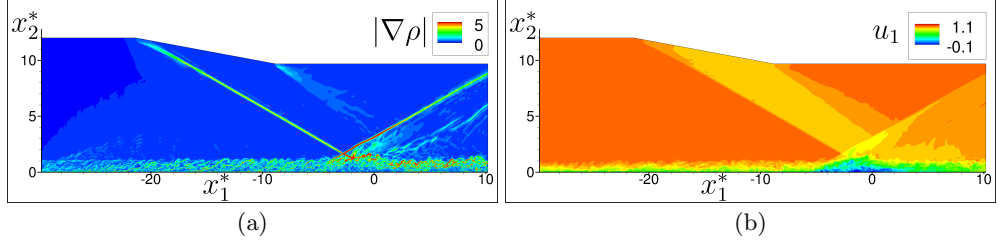


FIGURE 5. Turbulent shockwave boundary layer interaction at Mach  $M = 2.7$  and Reynolds number of  $Re_\delta = 54600$ , shown in terms of instantaneous flowfields of (a) the density gradient magnitude  $|\nabla \rho|$ , and (b) the streamwise velocity  $u_1$ .

spectral peaks appears as a repeating pattern, indicating potentially a signature pattern of the spectrogram for a stationary LDC flow at  $Re_L = 15000$ .

#### 4. Turbulent shockwave boundary layer interaction flow

Next, we consider a more complex flow configuration of shockwave turbulent boundary layer interaction to perform spacetime spectral analysis using SMD. The turbulent boundary layer flow is at a supersonic Mach number  $M = 2.7$  and Reynolds number of  $Re_\delta = 54600$  based on the inflow boundary layer thickness,  $\delta_{in}$ . An oblique incident shock at an angle of 30.29 deg impinges on the boundary layer, engendering SBLI. The incident shock is strong enough to produce flow separation, in the time-mean sense, giving rise to the characteristic low-frequency unsteadiness of SBLI as well as an increased level of turbulence.

The details of the flow configuration, computational domain, numerical grid, methodology along side the insights into the flow physics are provided in our prior works (Shinde *et al.* 2021; Shinde & Gaitonde 2022; Shinde 2025a). Briefly, the flow geometry is shown in Fig. 5(a), exhibiting flow structures in terms of the instantaneous density gradient magnitude ( $|\nabla \rho|$ ). The computational mesh consists of  $1201 \times 324 \times 481$  points in the streamwise, wall normal, and spanwise directions, respectively, with a total of  $\approx 187 \times 10^6$  grid points, resulting in a highly resolved LES database. The inflow is at  $x_1^* = -29.8$ , where an artificially generated turbulent boundary layer is introduced to the computation domain. A fully developed turbulent boundary layer is achieved by  $x_1^* = -21.3$ . The turbulent boundary layer enters into the SBLI region a few boundary layer thickness upstream the inviscid shock impingement location of  $x_1^* = 0$ . The incident shock causes a boundary layer separation of an extent  $\approx 5\delta_{in}$  all upstream of  $x_1^* = 0$ .

The key features of SBLI include: a low-frequency unsteadiness or breathing of the separation bubble, a separation shock that oscillates with the separation bubble, formation of a shear layer and its interaction with the incident shock, reattachment of the shear layer, generation of compression shocks post shock impingement location, and importantly the feedback from the reattachment to the separation region through the separation bubble (Dussauge *et al.* 2006; Touber & Sandham 2009a; Gaitonde 2015; Pasquariello *et al.* 2017; Shinde & Gaitonde 2022). In addition, SBLI typically leads to an increase of turbulence via distinct mechanisms in the upstream and the downstream regions of the shock impingement (Andreopoulos *et al.* 2000; Helm *et al.* 2014; Dupont *et al.* 2019; Shinde & Gaitonde 2022). As a result, SBLI manifest a wide range of length and time scales, involving hydrodynamics mechanisms that exhibit unsteadiness orders of magnitude lower compared to the scales of incoming turbulent boundary layer. In addition, there exist a mid-range frequency scales pertaining to the shear-layer vortical

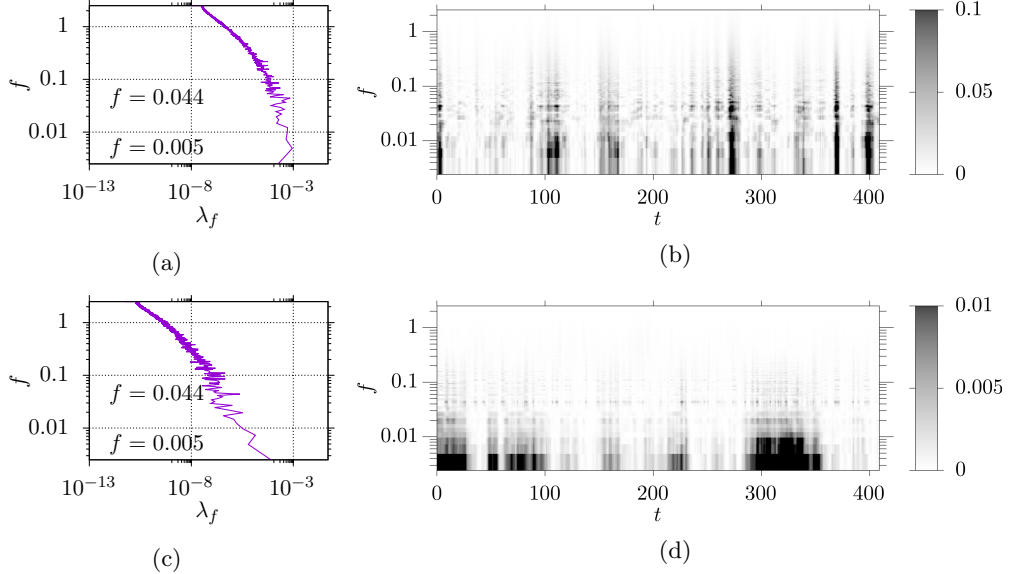


FIGURE 6. Global spectral energies ( $\lambda_f$ ) and spectrograms,  $|\varphi_f|^2$ , of the shockwave boundary layer interaction flow. (a) Spacetime integrated spectral energy of the streamwise velocity, (b) spectrogram of the streamwise velocity, (c) total spectral energy of the pressure, and (d) spectrogram of the pressure.

structures, as well as a higher-range frequency scales potentially involving acoustic mechanisms (Pirozzoli & Grasso 2006).

The spacetime-spectral analysis via spectral mode decomposition is expected to segregate the key features of SBLI, providing insights into the interplay among different scales. As noted before, SBLI comprises a wide range of scales including an order of magnitude low-frequency oscillations compared to the incoming turbulence. For the freestream velocity of  $u_\infty = 1$  and the inflow boundary layer thickness of  $\delta_{in} = 1$ , a turbulent boundary layer manifests non-dimensional frequencies about  $f \approx 1$ ; however, an SBLI with a flow separation length of  $L \approx 5\delta_{in}$  (such as the one considered here) engenders unsteadiness typically around  $f \approx 0.006$  (Clemens & Narayanaswamy 2014; Dussauge *et al.* 2006; Gaitonde 2015). Following the Nyquist criterion, a set of  $n = 4000$  snapshots with time step of  $\delta t = 0.1$  are gathered to perform SMD analysis. Also, the SMD is performed over the 2D mid-plane (as shown in Fig. 5) of the full 3D LES domain, treating the three components of velocity and the pressure. The large flowfields and their SMD require parallel computing, where we adopt the recent methodologies of parallelization presented in Shinde (2025a), albeit SMD does not involve solving for an eigenvalue problem. An instance of streamwise velocity is displayed in Fig. 5(b), indicating the SBLI region with a flow recirculation bubble.

The natural first step in SMD analysis of fluid flows is to examine the total spectral energies along side the spectrogram. These provide insights into the prominent spectral peaks of the flow as well as their temporal presence. The most energetic peaks and thus associated spatial modes can be then examined for the spatial appearance/structure of mode. Figure 6 displays the total spectral energies associated with SMD modes (on the left) and their spectrograms (on the right) for the streamwise velocity (in the top row) and the pressure (in the bottom row). As expected, the both spectra and spectrograms reveal a wide range of frequencies from less than  $f = 0.0025$  to  $f \approx 1$ . The classical low-

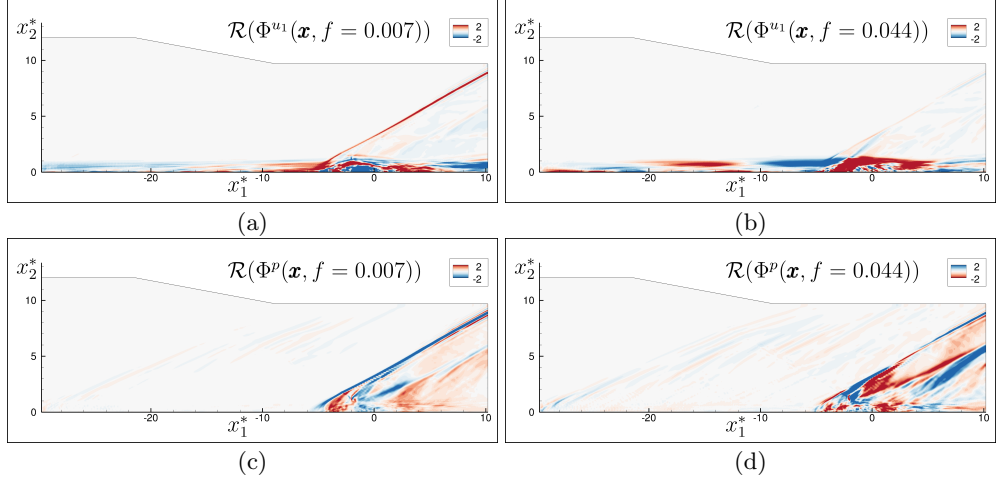


FIGURE 7. Spectral spatial modes of SBLI (real parts) for streamwise velocity (top row) and pressure (bottom row) at  $f = 0.007$  (of the left) and  $f = 0.44$  (on the right).

frequency peak at  $f \approx 0.006$  (which corresponds to  $f_L = 0.03$  in terms of the streamwise extent of flow separation,  $L$ ) is observable in both the spectrograms and the total spectra. A mid-range spectral peak at  $f \approx 0.044$  is evident in the figures for both the streamwise velocity (Fig. 6a,b) and the pressure (Fig. 6c,d). In addition, there are peripheral peaks in both in the higher/lower ranges of frequencies; however these are not prominent at least with the given spectral resolution.

The spectrograms of the streamwise velocity and the pressure bring out novel insights into SBLI in terms of the time synchronization of the different spectral peaks, and thus the spatial events in the SBLI. The low-frequency peaks generally correspond to the streamwise breathing motion of the separation bubble, whereas the mid-range frequency unsteadiness is generally attributed to the shear layer vortex shedding (Adler & Gaitonde 2018; Shinde & Gaitonde 2022). The intensity of the spectral peaks of the streamwise velocity spectrogram (Fig. 6b) increases for all ranges of frequencies at the same time but in an intermittent manner. The consistent presence of the mid-range spectral peak, which corresponds to the shear-layer vortex shedding, is evident in the both spectrograms. Furthermore, the peaks of low-frequency unsteadiness for the streamwise velocity and the pressure do not appear at the same time instance, suggesting a lag/phase dynamics between the velocity and the pressure fields.

The spectral spatial modes of SBLI that correspond to the spectral peaks at  $f = 0.007$  and  $f = 0.044$  are presented in Fig. 7, for the streamwise velocity (top row) and the pressure (bottom row). Since SBLI is the main driver of the low-frequency unsteadiness in this flow, the spatial modes are situated around  $x_1^* = 0$ , *i.e.* the shock impingement location. This is consistent with the modes of POD and DMD of SBLI, see for instance (Pasquariello *et al.* 2017; Nichols *et al.* 2017; Shinde & Gaitonde 2022; Shinde 2025a). The low frequency SMD mode at  $f = 0.007$  for the streamwise velocity delineates the flow separation region and the separation shock. In addition, the modal coherence is present in the downstream as well as much of the upstream region in the turbulent boundary layer. The second mode of streamwise velocity at  $f = 0.044$  also displays its presence in the upstream region of the SBLI. For the streamwise velocity fluctuations, it is long argued that the fluctuations in the upstream region of SBLI are the cause of SBLI low-frequency unsteadiness (Beresh *et al.* 2002; Adams 2000; Ganapathisubramani *et al.*

2009), albeit the causality is not evident here. The peaks of the pressure modes on the other hand are mainly situated in the separation and downstream regions (Fig. 7c,d). Notably the emanating shock off the SBLI are exhibited by the pressure modes, including the separation and compression shocks. The pressure mode dynamics is more aligned with the second mechanism of SBLI unsteadiness, which remains intrinsic to the separated flow and feedback from the reattachment to separation points (Dussauge *et al.* 2006; Piponnaiu *et al.* 2009; Touber & Sandham 2009b). The spacetime-spectral dynamics of other modes for the streamwise velocity and the pressure as well as the spanwise and wall normal velocity components is expected to reveal more about the physics of SBLI.

## 5. Full/reduced rank reconstruction of flowfields

Reconstruction of the original flowfields is an important facet of modal decomposition techniques. This generally involves a linear combination of select spatial modes and corresponding time coefficients. The modal reconstruction of flowfields enables various applications, including data reduction, denoising, reduced-order predictive modeling, among others. In this section, we present the reconstruction of flowfields using the SMD procedure, specifically utilizing Eq. 2.10. The real part of the tensor  $\mathbf{U}$  of Eq. 2.10 consists of the original real flowfields with no imaginary part. In reconstruction of  $\mathbf{U}$  however, the imaginary part may comprise machine-precision/discretization-related errors that can be neglected, unless the original flowfields had a non-zero imaginary part. The equation Eq. 2.10 can be expressed as,

$$\mathbf{U} = \sum_{n=1}^N \boldsymbol{\phi}_n \lambda_n^{\frac{1}{2}} \boldsymbol{\psi}_n^\dagger, \quad (5.1)$$

where  $N$  is the maximum number of spectral modes. The element-wise contribution of a particular spectral mode ( $n$ ) at a unique frequency ( $f$ ) in the reconstruction of  $\mathbf{U}$  can be given as

$$\mathcal{R}(U_{ij}) = \lambda^{\frac{1}{2}} [\mathcal{R}(\phi_i)\mathcal{R}(\psi_j) + \mathcal{I}(\phi_i)\mathcal{I}(\psi_j)], \text{ and} \quad (5.2)$$

$$\mathcal{I}(U_{ij}) = \lambda^{\frac{1}{2}} [\mathcal{I}(\phi_i)\mathcal{R}(\psi_j) - \mathcal{R}(\phi_i)\mathcal{I}(\psi_j)], \quad (5.3)$$

where  $\mathcal{R}$  and  $\mathcal{I}$  stand for real and imaginary parts, respectively.

The SMD reconstruction of the LDC flow at  $Re = 12000$  of Fig. 1(a) and the LDC flow at  $Re = 15000$  of Fig. 3(a) by means of Eq. 5.1 is presented in Fig. 8. It is a full reconstruction where all spectral modes are utilized. Fig. 8(a) and Fig. 8(c) display the reconstructed horizontal component of velocity in the LDC at  $Re = 12000$  and  $Re = 15000$ , respectively, where the reconstruction is at the same time instance of Fig. 1(a) and Fig. 3(a), respectively. The original and reconstructed LDC flowfields for both cases are indistinguishable visually. Furthermore, the flow velocity is compared at two probe locations, where the probes are located in the core vortex ( $P1$ ) and shear layer ( $P2$ ) regions of the LDC flow in both cases. The flow velocity at two probe locations are compared in Fig. 8(b) and Fig. 8(d). As expected, there is a good agreement between the original and reconstructed flows in both cases, with some local differences for LDC at  $Re = 15000$  at the probe in the shear layer region ( $P2$ ).

The full reconstruction (Eq. 5.1) of the SBLI flowfields is presented in Fig. 9 in terms of the streamwise velocity and the pressure fields. The instantaneous streamwise flow velocity in Fig. 9(a) is reconstructed at the exact same time instance as the velocity field shown in Fig. 5(b); again, the visual differences are minuscule. Fig. 9(b) shows the instantaneous pressure field reconstructed along side the velocity field for the same

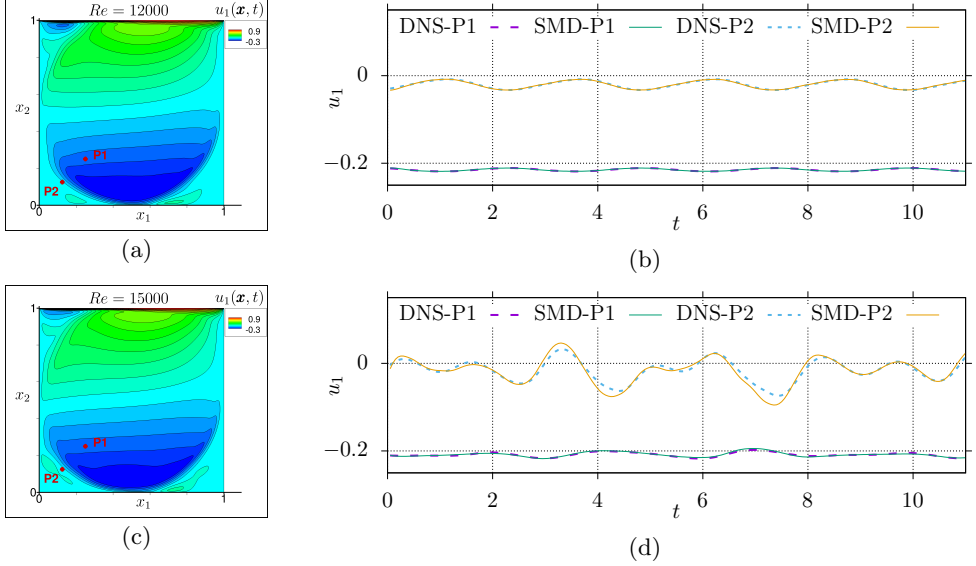


FIGURE 8. Reconstruction of the horizontal velocity flowfields from the SMD modes of LDC at  $Re = 12000$  and  $Re = 15000$ . (a) Reconstructed horizontal velocity field at the same time instance as in Fig. 1(a), (b) Comparison of the space-point time-variation of the horizontal velocity between DNS and SMD-reconstructed flowfield at the probe locations:  $P1 = (0.25, 0.25)$  and  $P2 = (0.125, 0.125)$

instance. It also agrees well with the original pressure field at that time instance. To compare the reconstructed flowfields at a probe location, we consider a probe close to the shock impingement location, at  $(x_1^* = 0.17, x_2^* = 0.1)$ , where the flow is highly turbulent. The original and reconstructed flowfields at this probe location are displayed in Fig. 9(c) for the streamwise velocity and Fig. 9(d) for the pressure. The comparison shows a good agreement for the both variables particularly in terms of the spectral content, while some discrepancies show up for the streamwise velocity in terms of the instantaneous amplitudes. The potential reasons for these differences include the difference of temporal resolution between the LES ( $\delta t = 0.001$ ) and the dataset used ( $\delta t = 0.1$ ) as well as the lower number of snapshots ( $N = 4000$ ) employed, given the presence of low-frequency unsteadiness in SBLI.

To improve the spectral convergence, Welch method (Welch 2003) is commonly used, where a full length signal is divided into multiple time windows leading to an averaged spectrum. In addition, the alteration of time signal to avoid spectral leakage, the ensemble averaging, and/or the zero padding of signal are some practical operations to improve the accuracy and computational efficiency of the time-frequency transformation. However, this typically results in the phase information loss, making the reconstruction of the original flowfields a tedious task. For instance, the conventional spectrograms lose phase information during repeated application of the short time Fourier transform (STFT), retaining only the magnitude information. In contrast, the SMD spectrogram of the non-normalized spectral time-modes  $|\varphi_f|^2$  essentially utilizes the spectral energies and the spectral time modes, which are obtained by an oblique projection of the flowfields on the spectral spatial-modes. Thus, the reconstruction of  $\mathbf{U}$  in Eq. 5.1, consisting Eq. 5.2 and Eq. 5.3, inherently retains the spectral phase information without any explicit calculation for the modal phase.

To elaborate on the loss of phase information, we can consider the reconstruction of  $\mathbf{U}$

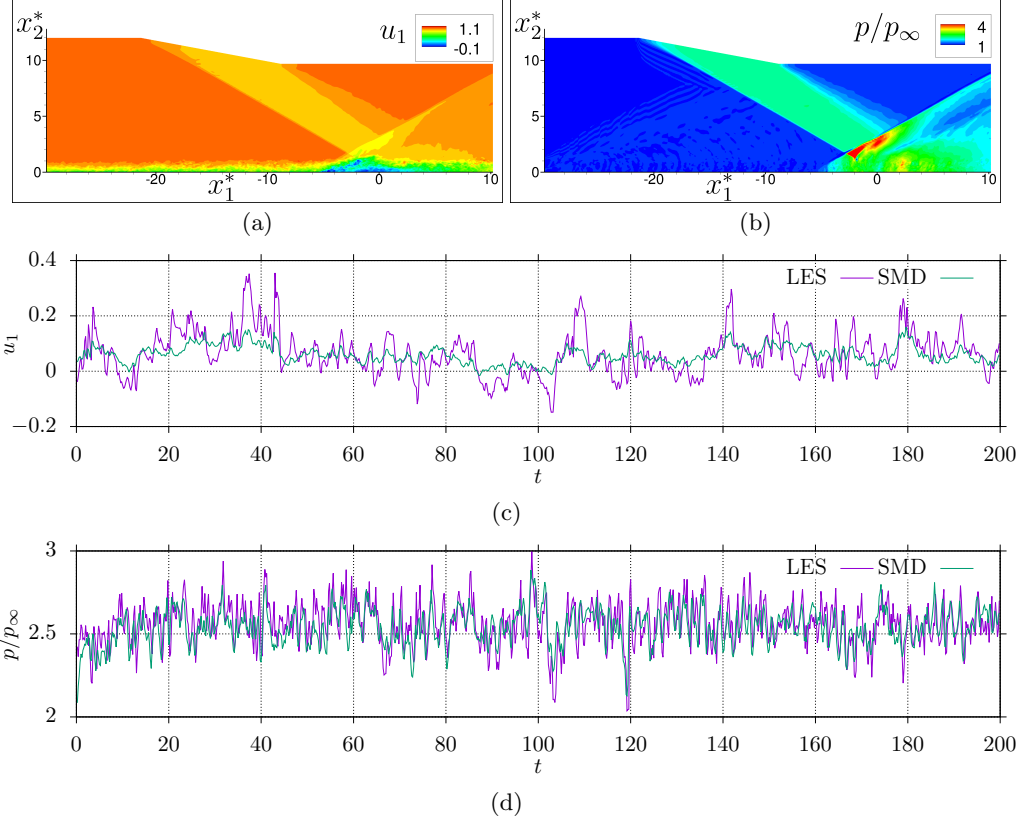


FIGURE 9. Reconstruction of SBLI instantaneous flowfields using SMD procedure for (a) the streamwise velocity and (b) the pressure. Comparison of the instantaneous (c) streamwise velocity and (d) pressure near the shock impingement location (probe at  $x_1^* = 0.17$ ,  $x_2^* = 0.1$ ) between the LES and SMD.

in terms of the phase ( $\Theta$ ) of the spectral modes, given as

$$\Theta = \arctan(\mathcal{I}(\Phi), \mathcal{R}(\Phi)). \quad (5.4)$$

Equations 5.2 and 5.3, which provide the element-wise contribution of a spectral mode at a frequency  $f$  in the reconstruction of  $\mathbf{U}$ , can be expressed in terms of the phase as

$$\mathcal{R}(U_{ij}) = |\phi_i \lambda^{\frac{1}{2}} \psi_j^\dagger| \cos(2\pi f t + \Theta_i), \text{ and} \quad (5.5)$$

$$\mathcal{I}(U_{ij}) = |\phi_i \lambda^{\frac{1}{2}} \psi_j^\dagger| \sin(2\pi f t + \Theta_i) \quad (5.6)$$

The LDC and SBLI flowfields that are reconstructed by employing the phase-based approach (of Eqs. 5.5 and 5.6) along side the projection-based approach (of Eqs. 5.2 and 5.3) are presented in Fig. 10. For these reconstructions, the spectral spatial-modes are obtained by taking an ensemble average of spectra that are computed over multiple time windows, anticipating a phase loss. The graphs of Fig. 10 use ‘#’ symbol to indicate the number of time windows used to perform the ensemble average of spectra. The Welch method here employs a rectangular window with no overlap.

Figures 10(a) and 10(b) display the velocity probe ( $P2$ ) data that are reconstructed using the phase and projection based approaches, respectively, for the LDC at  $Re = 15000$ . Clearly, the phase-based reconstruction of the horizontal velocity (Fig. 10a) deteriorate as the spectral spatial-modes are averaged over more number of time windows.

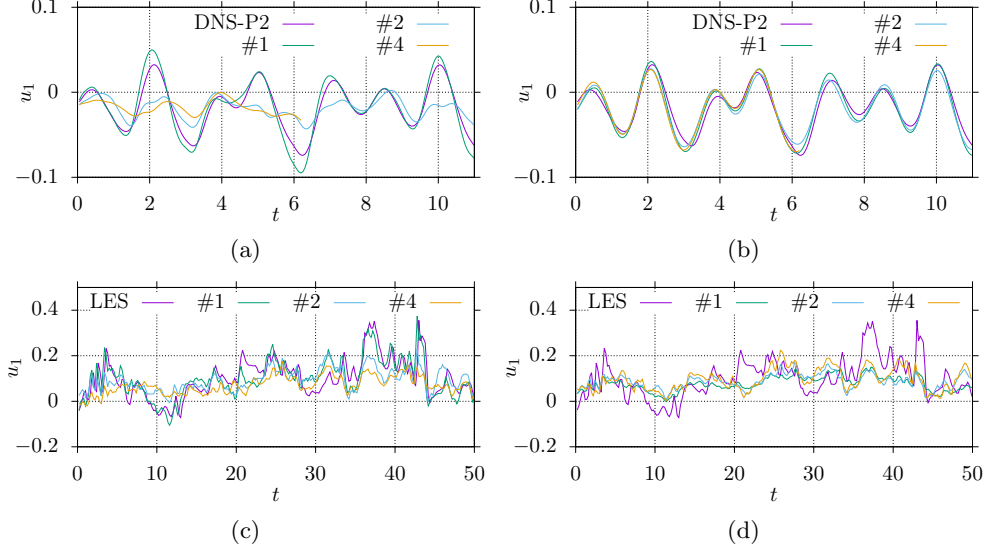


FIGURE 10. Effect of spectral spatial mode convergence on the reconstruction of flowfields. (a) Phase-based and (b) projection-based reconstruction of the horizontal velocity at probe  $P2$  in LDC at  $Re = 15000$ . (c) Phase-based and (d) projection-based reconstruction of the streamwise velocity near the shock impingement location (at  $x_1^* = 0.17$ ,  $x_2^* = 0.1$ ) in SBLI. The graph titles with symbol  $\#$  and a following number indicate the number of blocks used in the spectral averaging of SMD spatial modes.

In contrast, the projection-based reconstruction (Fig. 10b) accurately predicts the time variation of the velocity for all number of time windows:  $\#1$ ,  $\#2$ , and  $\#4$ . Note that although  $\#2$  and  $\#4$  cases comprise small time windows, these resolve all frequencies present in the flow. In the case of SBLI, there exist much lower flow frequencies compared to the resolved frequencies even for the longer time window of  $\#1$ . Nonetheless, the phase-based reconstruction of the SBLI flow (of Fig. 9c, in terms of the streamwise velocity probe near the shock impingement location) remains consistent, and deteriorates with the spectral averaging operation. The projection-based reconstruction of the SBLI flow (of Fig. 9d) also shows similar trend, where the increasing number of time windows has an effect on the reconstructed flowfields. However, the reconstructed 2D flowfields (not shown) by using the projection-based approach provide more accurate solution, particularly under the spectral averaging operation.

A partial reconstruction of flowfields finds applications in data size reduction, denoising, reduced-order modeling (ROM), among others. Modal decomposition techniques are popularly utilized in ROM of fluid flows, where a set of select modes lead to an efficient model that governs the system dynamics. Linearity of the modes is an important property of a modal decomposition technique, allowing linear combinations of the essential modes while discarding the unnecessary modes of the system dynamics. SMD inherits the linearity from Fourier transform. For instance, the reconstruction of flowfields in Eq. 5.1 represents a linear combination of the spectral modes and energies. The mode selection in SMD for a partial reconstruction of flowfields is straightforward, where energy and/or frequency or their ranges can be used as the selection criteria.

The spectral energies of the LDC flow at  $Re = 50000$  and the SBLI are presented in Fig. 11, where the modal energies are associated with both the frequency ( $f$ ) and the energy rank ( $n$ ). The modal energies,  $\lambda_f$  and  $\lambda_n$ , are shown on  $y$ -axis on a logarithmic scale. The frequency and the modal rank use  $x$ -axis on a logarithmic scale and  $x2$ -axis on

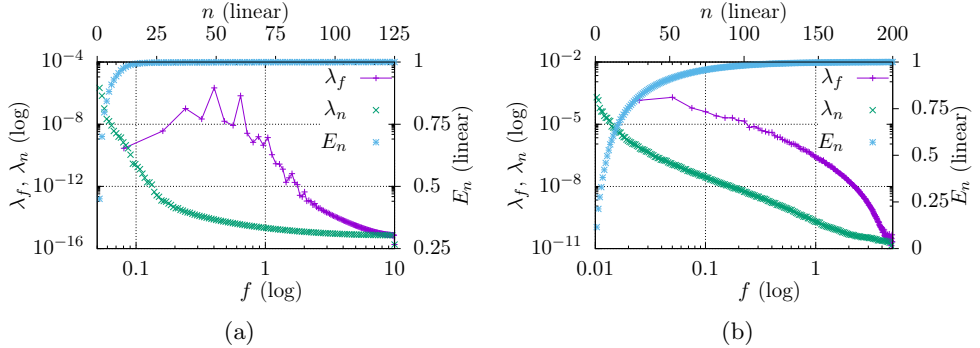


FIGURE 11. Spectral modal energy as a function of frequency and mode number for (a) LDC at  $Re = 15000$ , and (b) SBLI.  $E_n = \sum_{l=1}^n \lambda_l / \sum_{l=1}^N \lambda_l$  is a normalized cumulative energy of the modes.

a linear scale, respectively. The sub-figures also present a total cumulative energy ( $E_n$ ) graph for increasing modal rank as:

$$E_n = \frac{\sum_{l=1}^n \lambda_l}{\sum_{l=1}^N \lambda_l}, \quad (5.7)$$

on  $y2$ -axis in a linear scale. The spectral variation versus frequency is evident, where for LDC flow (Fig. 11a) most of the spectral energy is associated with the modes with  $f \lesssim 1$  with a peak at  $f = 0.38$ . On the other hand, the SBLI is a fully turbulent flow with a considerable spectral energy distribution at the higher (relative to the lower frequencies of SBLI) turbulent frequencies as well. The spectral energies with energy rank  $\lambda_n$  clearly show that almost all energy is associated with less than 50% modes. The energy graph of LDC flow (Fig. 11a) shows only 12 out of 125 modes (*i.e.*,  $\approx 10\%$  modes) contain more than 98% of the total energy. For the SBLI flow (Fig. 11b) the first 10% modes comprise  $\approx 85\%$  of the total modal energy, indicating a higher rank flow compared to the LDC flow.

The partial reconstructions of the LDC at  $Re = 15000$  and SBLI flows are displayed in Fig. 12 by reducing the number modes used in the flowfields reconstruction. For LDC flow, the reconstruction is performed using 100%, 5%, and 2% of the total modes that are ranked by energy. The results in terms of the horizontal velocity (Fig. 11a) show a decrease of signal energy for decreasing the number of modes in the reconstruction, with no loss of phase information. The full horizontal velocity flowfield is displayed in Fig. 11(c) for the 2%-modes reconstruction, which exhibits minimal differences in the flow (in the shear layer region) compared to the DNS field of Fig. 3(a). In the case of SBLI flow, the partial reconstruction is performed using 100%, 20%, and 5% of the total modes that are ranked by energy. Figure 11(b) shows the reconstruction results in terms of the streamwise velocity at the probe ( $x_1^* = 0.17$ ,  $x_2^* = 0.1$ ) near the shock impingement location. The turbulent response of the LES and 100% reconstruction is evident in the figure; in addition, as the percentage of modes decreased to 5% the velocity graph became smoother. The SBLI instantaneous velocity flowfield for 5% mode reconstruction is shown in Fig. 11(d), clearly showing the filtering out of the turbulent features of the flow.

## 6. Concluding remarks

This paper presents a spectral mode decomposition technique to perform spacetime-frequency analysis of spatiotemporal flowfields. While the techniques for time-frequency

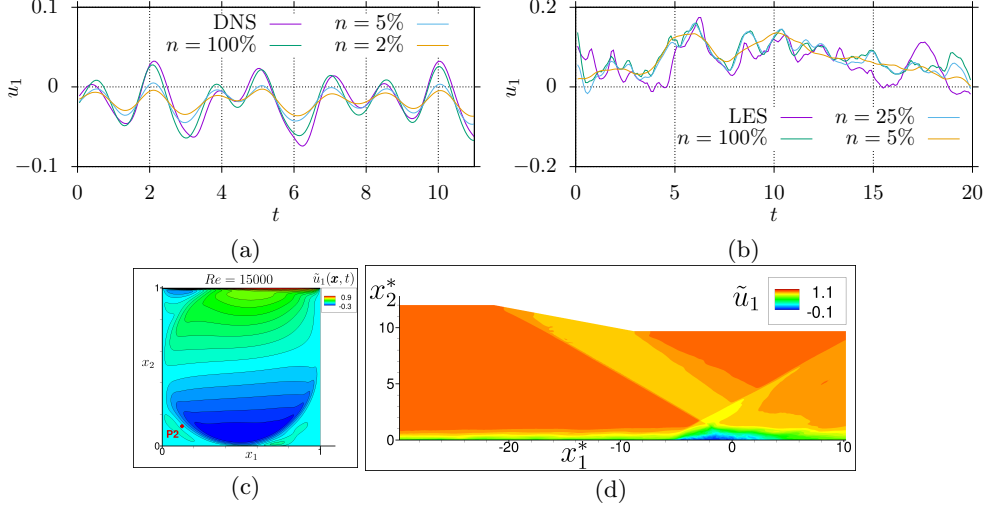


FIGURE 12. Reduced order flowfield reconstruction using SMD. (a) Instantaneous horizontal velocity (at probe  $P2$ ) in LDC at  $Re = 15000$ , and (b) the streamwise velocity at a probe ( $x_1^* = 0.17$ ,  $x_2^* = 0.1$ ) near the shock impingement location in SBLI. Reconstruction of (c) LDC and (d) SBLI flowfields with a reduced number of modes, respectively, 2% and 5% of the total number of modes.

analysis and frequency-based modal decomposition are fairly well established in the literature, broadly these techniques have been treating the problems for either time-locality of the spectrum or a converged spatial coherence of the spectral modes. In fluid dynamics, where high resolution spatiotemporal experimental and numerical databases are commonly encountered, a combined treatment of spatiotemporal dynamics is highly desired; the presented SMD approach precisely addresses this point. The existing frequency-based modal decompositions, mainly the FT, DMD, and the spectral variants of POD, consider a constant frequency time-variation of the modal time-coefficients or equivalently the modal contribution over time. This is questionable, particularly in turbulent flowfields. Besides, the main objective of the time-frequency analysis techniques is precisely to obtain that time-local contribution/presence of frequency. This time-local spectral presence and its variation over time need not be at the same constant frequency.

The SMD procedure distills out three main features of the spatiotemporal flowfields: 1) the spectral spatial modes that correspond to a unique frequency; thus, a unique spectral mode at a unique frequency. 2) The spectral time-modes (time-coefficients) exhibit the time-local contribution/presence of the corresponding spectral spatial mode. While the time-modes correspond to the unique frequency spatial modes, their time-local contribution need not be constant over time at the modal frequency, instead it depends on the instantaneous physical process in the flowfield. The non-normalized time-modes lead to a time-resolved contribution of the spectral modes, well known as the spectrogram. A peak on the spectrogram indicates the presence of that global mode at that specific time, providing crucial insights into the physical mechanisms of unsteadiness in the flow. 3) Lastly, the spectral modes are associated with a global spectral energy, which unambiguously defines the energy rank of the mode. In addition to the modal frequency, the energy rank provides another convenient mode selection criterion, where the both criteria are useful in full/partial reconstruction of the flowfields, reduced-order modeling and de-noising applications.

Application of SMD to transitional (LDC at Mach 0.5 and  $Re_L = 12000$ )/turbulent

(LDC at Mach 0.5 and  $Re_L = 15000$  and SBLI at Mach 2.7 and  $Re_{\delta_{in}} = 54666$ ) flows manifest how conveniently SMD extracts the spectral modes that are energy dominant and their temporal presence in the flow. In transitional flows, where the unsteadiness/instabilities are dictated by a relatively fewer number of spectral modes, SMD is particularly useful in tracing the spatiotemporal presence of those modes. Similarly in turbulent flows, SMD can easily trace intermittent/extreme events and provide insight into their spatiotemporal presence and modal support. For instance, the SMD spectrograms of the SBLI flow clearly exhibit the spectral energy peaks/bursts at the characteristic lower frequency range of SBLI. Notably, the low-frequency peaks of the pressure and the streamwise velocity appear at different time instances (Figs. 6b & 6d), indicating the difference in dynamics at the low-frequency range of SBLI for different variables (at least for the pressure and the streamwise velocity here). A further detailed investigation of this temporal dynamics by considering the wall normal/spanwise velocity and temperature is expected to shed more light on the mechanisms of low-frequency unsteadiness in SBLI.

Lastly, the convergence of the spectral modes is generally enhanced by means of ensemble averaging or by employing Welch method (Welch 2003), where a long duration statistically stationary signal is divided into small-duration windows. Other practical modifications to time signals include the shapes of windows (*e.g.* Hanning window) to control spectral leakage, and/or the zero padding to improve the algorithm efficiency. The phase information is generally compromised in these operations. To this end, employing the projection-based SMD reconstruction provides better results compared to the phase-based SMD reconstruction of the flowfields. The paper also illustrates the use of SMD in full/partial flow reconstruction based on modes at a specific frequency/energy or their ranges. The use of SMD in reduced-order modeling deserves further investigation, as it must deal with the non-orthogonality of modes.

## Acknowledgment

This work is supported by the National Aeronautics and Space Administration (NASA) under Grant No. 80NSSC24M0103. The author acknowledges the computing resources provided by the high performance computing collaboratory (HPCC) of Mississippi State University.

## REFERENCES

- ADAMS, N. A. 2000 Direct simulation of the turbulent boundary layer along a compression ramp at  $m=3$  and  $re\theta=1685$ . *Journal of Fluid Mechanics* **420**, 47–83.
- ADLER, M. C. & GAITONDE, D. V. 2018 Dynamic linear response of a shock/turbulent-boundary-layer interaction using constrained perturbations. *Journal of Fluid Mechanics* **840**, 291–341.
- ALBENSOEDER, S. & KUHLMANN, H. C. 2005 Accurate three-dimensional lid-driven cavity flow. *Journal of Computational Physics* **206** (2), 536–558.
- ANDREOPoulos, Y., AGUI, J. H. & BRIASSULIS, G. 2000 Shock wave–turbulence interactions. *Annual review of fluid mechanics* **32** (1), 309–345.
- BATCHELOR, G. K. 1953 *The theory of homogeneous turbulence*. Cambridge university press.
- BERESH, S., CLEMENS, N. & DOLLING, D. 2002 Relationship between upstream turbulent boundary-layer velocity fluctuations and separation shock unsteadiness. *AIAA journal* **40** (12), 2412–2422.
- BERGAMO, L. F., GENNARO, E. M., THEOFILIS, V. & MEDEIROS, M. A. F. 2015 Compressible modes in a square lid-driven cavity. *Aerospace Science and Technology* **44**, 125–134.

BRUNEAU, C.-H. & SAAD, M. 2006 The 2d lid-driven cavity problem revisited. *Computers & fluids* **35** (3), 326–348.

CLEMENS, N. T. & NARAYANASWAMY, V. 2014 Low-frequency unsteadiness of shock wave/turbulent boundary layer interactions. *Annual Review of Fluid Mechanics* **46**, 469–492.

COHEN, L. 1995 Time-frequency analysis. *Englewood Cliffs* .

DUPONT, P., PIPONNIAU, S. & DUSSAUGE, J. 2019 Compressible mixing layer in shock-induced separation. *Journal of Fluid Mechanics* **863**, 620–643.

DUSSAUGE, J.-P., DUPONT, P. & DEBIEVE, J.-F. 2006 Unsteadiness in shock wave boundary layer interactions with separation. *Aerospace Science and Technology* **10** (2), 85–91.

GAITONDE, D. V. 2015 Progress in shock wave/boundary layer interactions. *Progress in Aerospace Sciences* **72**, 80–99.

GANAPATHISUBRAMANI, B., CLEMENS, N. & DOLLING, D. 2009 Low-frequency dynamics of shock-induced separation in a compression ramp interaction. *Journal of Fluid Mechanics* **636**, 397–425.

GHIA, U., GHIA, K. N. & SHIN, C. T. 1982 High-re solutions for incompressible flow using the navier-stokes equations and a multigrid method. *Journal of computational physics* **48** (3), 387–411.

HELM, C., MARTIN, M. P. & DUPONT, P. 2014 Characterization of the shear layer in a mach 3 shock/turbulent boundary layer interaction. In *Journal of Physics: Conference Series*, , vol. 506, p. 012013. IOP Publishing.

KOSEFF, J. R., STREET, R. L., GRESHO, P. M., UPSON, C. D., HUMPHREY, J. A. C. & TO, W. M. 1983 Three-dimensional lid-driven cavity flow: experiment and simulation. *Tech. Rep.* Stanford Univ., CA (USA). Dept. of Civil Engineering; Lawrence Livermore ....

LOPEZ, J. M., WELFERT, B. D., WU, K. & YALIM, J. 2017 Transition to complex dynamics in the cubic lid-driven cavity. *Physical Review Fluids* **2** (7), 074401.

LUMLEY, J. L. 1967 The Structure of Inhomogeneous Turbulent Flows. In *Atmospheric turbulence and radio propagation* (ed. A. M. Yaglom & V. I. Tatarski), pp. 166–178. Moscow: Nauka.

LUMLEY, J. L. 1970 *Stochastic tools in turbulence*. Academic Press.

MORALES, S. & BOWERS, M. E. 2022 Time-frequency analysis methods and their application in developmental eeg data. *Developmental cognitive neuroscience* **54**, 101067.

NEKKANTI, A. & SCHMIDT, O. T. 2021 Frequency–time analysis, low-rank reconstruction and denoising of turbulent flows using spod. *Journal of Fluid Mechanics* **926**, A26.

NICHOLS, J. W., LARSSON, J., BERNARDINI, M. & PIROZZOLI, S. 2017 Stability and modal analysis of shock/boundary layer interactions. *Theoretical and Computational Fluid Dynamics* **31** (1), 33–50.

OHMICHI, Y. & SUZUKI, K. 2017 Compressibility effects on the first global instability mode of the vortex formed in a regularized lid-driven cavity flow. *Computers & Fluids* **145**, 1–7.

PASQUARIELLO, V., HICKEL, S. & ADAMS, N. A. 2017 Unsteady effects of strong shock-wave/boundary-layer interaction at high reynolds number. *Journal of Fluid Mechanics* **823**, 617–657.

PIPONNIAU, S., DUSSAUGE, J., DEBIEVE, J. & DUPONT, P. 2009 A simple model for low-frequency unsteadiness in shock-induced separation. *Journal of Fluid Mechanics* **629**, 87–108.

PIROZZOLI, S. & GRASSO, F. 2006 Direct numerical simulation of impinging shock wave/turbulent boundary layer interaction at  $m= 2.25$ . *Physics of Fluids* **18** (6), 065113.

RAMANAN, N. & HOMSY, G. M. 1994 Linear stability of lid-driven cavity flow. *Physics of Fluids* **6** (8), 2690–2701.

RAMANAN, N., UNNIKRISHNAN, S. & GAITONDE, D. 2020 A robust approach for stability analysis of complex flows using high-order navier-stokes solvers. *Journal of Computational Physics* **403**, 109076.

ROWLEY, C. W. & DAWSON, S. T. 2017 Model reduction for flow analysis and control. *Annual Review of Fluid Mechanics* **49**, 387–417.

ROWLEY, C. W., MEZIĆ, I., BAGHERI, S., SCHLATTER, P. & HENNINGSON, D. 2009 Spectral analysis of nonlinear flows. *Journal of fluid mechanics* **641** (1), 115–127.

SCHMID, P. J. 2010 Dynamic mode decomposition of numerical and experimental data. *Journal of fluid mechanics* **656**, 5–28.

SHEN, J. 1991 Hopf bifurcation of the unsteady regularized driven cavity flow. *Journal of Computational Physics* **95** (1), 228–245.

SHEU, T. W. H. & TSAI, S. F. 2002 Flow topology in a steady three-dimensional lid-driven cavity. *Computers & fluids* **31** (8), 911–934.

SHINDE, V. 2025a Distributed-parallel proper orthogonal/dynamic mode decompositions of large flow data. *Computer Physics Communications* p. 109644.

SHINDE, V. J. 2025b Lagrangian stability analysis technique for fluid flows. *arXiv preprint arXiv:2509.10316*.

SHINDE, V. J. & GAITONDE, D. V. 2021 Lagrangian approach for modal analysis of fluid flows. *Journal of Fluid Mechanics* **928**, A35.

SHINDE, V. J. & GAITONDE, D. V. 2022 Features of oblique shock wave turbulent boundary layer interaction. In *AIAA SciTech 2022 Forum*, p. 1975.

SHINDE, V. J., GAITONDE, D. V. & McNAMARA, J. J. 2021 Supersonic turbulent boundary-layer separation control using a morphing surface. *AIAA Journal* **59** (3), 912–926.

SIEBER, M., PASCHERAIT, C. O. & OBERLEITHNER, K. 2016 Spectral proper orthogonal decomposition. *Journal of Fluid Mechanics* **792**, 798–828.

SIROVICH, L. 1987 Turbulence and the dynamics of coherent structures. part i: Coherent structures. *Quaterly of Applied Mathematics* **XLV** (3), 561–571.

TAIRA, K., BRUNTON, S. L., DAWSON, S. T., ROWLEY, C. W., COLONIUS, T., McKEON, B. J., SCHMIDT, O. T., GORDEYEV, S., THEOFILIS, V. & UKEILEY, L. S. 2017 Modal analysis of fluid flows: An overview. *Aiaa Journal* **55** (12), 4013–4041.

TENNEKES, H. & LUMLEY, J. L. 1972 *A first course in turbulence*. MIT press.

TOUBER, E. & SANDHAM, N. D. 2009a Comparison of three large-eddy simulations of shock-induced turbulent separation bubbles. *Shock Waves* **19** (6), 469.

TOUBER, E. & SANDHAM, N. D. 2009b Large-eddy simulation of low-frequency unsteadiness in a turbulent shock-induced separation bubble. *Theoretical and Computational Fluid Dynamics* **23** (2), 79–107.

TOWNE, A., SCHMIDT, O. T. & COLONIUS, T. 2018 Spectral proper orthogonal decomposition and its relationship to dynamic mode decomposition and resolvent analysis. *Journal of Fluid Mechanics* **847**, 821–867.

WELCH, P. 2003 The use of fast fourier transform for the estimation of power spectra: A method based on time averaging over short, modified periodograms. *IEEE Transactions on audio and electroacoustics* **15** (2), 70–73.